SCIENTIFIC REPORTS

OPEN

Intrinsic Origins of Crack Generation in Ni-rich $LiNi_{0.8}Co_{0.1}Mn_{0.1}O_2$ Layered Oxide Cathode Material

Received: 18 July 2016
Accepted: 10 November 2016
Published: 03 January 2017

Jin-Myoung Lim[1], Taesoon Hwang[1], Duho Kim[1], Min-Sik Park[2], Kyeongjae Cho[1,3] & Maenghyo Cho[1]

Ni-rich $LiNi_{0.8}Co_{0.1}Mn_{0.1}O_2$ layered oxide cathodes have been highlighted for large-scale energy applications due to their high energy density. Although its specific capacity is enhanced at higher voltages as Ni ratio increases, its structural degradation due to phase transformations and lattice distortions during cycling becomes severe. For these reasons, we focused on the origins of crack generation from phase transformations and structural distortions in Ni-rich $LiNi_{0.8}Co_{0.1}Mn_{0.1}O_2$ using multiscale approaches, from first-principles to meso-scale phase-field model. Atomic-scale structure analysis demonstrated that opposite changes in the lattice parameters are observed until the inverse Li content $x = 0.75$; then, structure collapses due to complete extraction of Li from between transition metal layers. Combined-phase investigations represent the highest phase barrier and steepest chemical potential after $x = 0.75$, leading to phase transformations to highly Li-deficient phases with an inactive character. Abrupt phase transformations with heterogeneous structural collapse after $x = 0.81$ (~220 mAh g^{-1}) were identified in the nanodomain. Further, meso-scale strain distributions show around 5% of anisotropic contraction with lower critical energy release rates, which cause not only micro-crack generations of secondary particles on the interfaces between the contracted primary particles, but also mechanical instability of primary particles from heterogeneous strain changes.

Ni-rich transition metal layered oxides ($LiNi_xCo_yMn_{1-x-y}O_2$, with $x > 0.5$, Ni-rich NCM) have been spotlighted during the past decade as the most promising candidates for high capacity cathode materials in Li-ion batteries (LIBs) due to their high energy densities (>200 mAh g^{-1} until ~4.6 V *vs.* Li/Li^+)[1–3]. Although $LiNi_{1/3}Co_{1/3}Mn_{1/3}O_2$ (NCM111) has been successfully commercialized, in order to meet the demand for large-scale energy storage applications such as electric vehicles (EVs) and energy storage systems (ESSs), further NCM research and development have been directed toward enhancing its specific capacity by increasing the ratio of the Ni component toward $LiNi_{0.8}Co_{0.1}Mn_{0.1}O_2$ (NCM811)[4–6].

While the increase of the Ni ratio in NCM contributes to an enhanced specific discharge capacity, it also results in severe capacity degradation caused by cation mixing, surface side reactions, and crack propagation with structural instability[1]. To better understand these challenges, Jung *et al.* investigated the degradation mechanism of the phase transformation induced by cation mixing from the surface to bulk using *ex situ* structural analysis[7]. Similarly, Lin *et al.* described the surface reconstruction and chemical evolution of the rhombohedral layered structure to a cubic spinel structure using high-throughput X-ray absorption spectroscopy[8]. As theoretical approaches, electronic correlations for the redox reactions between the multivalent transition metals in the Ni-rich NCM[9] and stability analysis with respect to the various ratios of the Ni, Co, and Mn components in the NCM[10] have been performed through first-principles calculations. On the bases of these fundamental data, many researchers have suggested solutions to resolve the cyclic degradation problem. Along with diverse approaches such as morphology control[11], elemental doping[12–15] and surface coating[16–20], Sun *et al.* have suggested various effective ways to reduce cyclic degradation and improve electrochemical performance through the design of core-shell[21], gradient core-shell[3,22], and full concentration gradient structures[2,23,24] for Ni-rich NCM cathodes.

[1]Department of Mechanical and Aerospace Engineering, Seoul National University, 1 Gwanak-ro, Gwanak-gu, Seoul 08826, Republic of Korea. [2]Department of Advanced Materials Engineering for Information and Electronics, Kyung Hee University, 1732 Deogyeong-daero, Giheung-gu, Yongin 17104, Republic of Korea. [3]Department of Materials Science and Engineering and Department of Physics, University of Texas at Dallas, Richardson, TX 75080, USA. Correspondence and requests for materials should be addressed to M.C. (email: mhcho@snu.ac.kr)

Nevertheless, micro-crack propagation in the secondary particle related to structural instability remains problematic, although cation mixing and surface deterioration can be prevented through the above-mentioned approaches. Among the promising Ni-rich compounds, severe structural changes and crack propagation have been observed experimentally in $LiNi_xCo_yAl_{1-x-y}O_2$ (NCA) cathodes[25–28]. Although, Meng *et al.* recently reported the experimental observation of micro-crack generation of NCM811 with severe cyclic degradation and suggested surface coating with Li_2TiO_3 to mitigate the crack propagation[29], the fundamental origin has not been adequately addressed for the Ni-rich NCM cathodes[1]. Moreover, the underlying mechanism for the phase transformation and structural changes in NCM811 is not fully understood. For these reasons, we focused on the study of intrinsic characteristics of the phase transformation and structural changes of NCM811 to elucidate its inherent structural instability regardless of cation mixing and surface deterioration.

Through multiscale phase-transformation mechanics based on first-principles calculations, here, we investigated the fundamental reaction mechanism, structural distortions, thermodynamic combined-phase (CP) behaviours, and meso-scale phase-separation kinetics for NCM811 with respect to varying Li concentration. Since the redox reactions during cycling mainly involve the Ni and O ions, the Co and Mn ions would retain similar electronic structures before and after delithiation. Anisotropic structural changes are observed between the *ab* plane and *c* axis, which result in anisotropic shrinkage of the entire structure. In particular, an abrupt collapse of the structure is observed for an inverse Li content $x = 0.75–1.0$ in $Li_{1-x}Ni_{0.8}Co_{0.1}Mn_{0.1}O_2$. The CP behaviour shows generally one-phase reactions with lower phase barriers below $x = 0.75$. However, a two-phase region with a remarkably higher phase barrier is presented after $x = 0.75$ and inactive phases are formed, which not only agrees well with the experiments of Ohzuku *et al*[30]. but also correlates with the collapse of the structure after $x = 0.75$. Based on these first-principles calculation results, meso-scale phase separation simulations were performed, which reveals heterogeneous phase transformations and structural changes at different Li concentrations. Therefore, an intrinsic limitation of NCM811 exists in the region $x = 0.75–0.81$ (~220 mAh g^{-1}) due to the inactive phase separation and abrupt structural changes. Around 5% of the anisotropic contraction was observed in the nanodomain, which induces the contractions of the primary particles. In addition, very low critical energy release rates for crack generation of fully-lithiated and delithiated NCM811 were calculated. Such large volume reduction and low critical energy release rate could be the reason of causing the micro-crack generations in the secondary particles on the interfaces between the contracted primary particles. Further, the heterogeneous strain changes cause severe mechanical instability within the primary particles, which could be the reason of the generation of nano-cracks as a seed of the micro-cracks. These findings should provide helpful insights for the development of Ni-rich NCM cathode materials in the Li-ion battery research community.

Results and Discussion

Redox Mechanism and Structural distortion. Figure 1a and b show the atomic model used for the first-principles calculations projected on the *bc* and *ab* planes, respectively. The atomic model was developed based on the rhombohedral layered oxide structure (*R*-3*m*) of $LiNiO_2$ (Inorganic Crystal Structure Database (ICSD) ID: 10499). To represent the stoichiometry of NCM811, supercells of $2 \times 2 \times 1$ with 12*f.u.* were used; the exact stoichiometry of the supercell in this study is $LiNi_{0.8333}Co_{0.0833}Mn_{0.0833}O_2$ ($Li_{12}Ni_{10}Co_1Mn_1O_{24}$). The model was developed using high-throughput calculations based on previously described schemes[31–35]. As shown in Fig. 1a, Co and Mn are located separately in the Ni-rich environment of the layered oxide structure, which would be thermodynamically related to *d*-electronic stability of the crystal field[36,37].

Figure 2 presents the partial (projected) density of states (PDOSs) of the Ni, Co, and Mn *d*-orbitals and the O *p*-orbitals in $Li_1Ni_{0.8}Co_{0.1}Mn_{0.1}O_2$ and $Li_0Ni_{0.8}Co_{0.1}Mn_{0.1}O_2$ (Fig. 2a–d and 2e–h, respectively). In the fully lithiated state ($Li_1Ni_{0.8}Co_{0.1}Mn_{0.1}O_2$), the Ni, Co, and Mn *d*-orbitals are shown as Ni^3-like, Co^{3+}, and Mn^{4+}-like shapes due to the effect of the *d*-electronic donor[9,38], in agreement with a previous report[10]. The thermodynamic stability of the Co^{3+} and Mn^{4+} crystal fields could be satisfied by maintaining their separate locations. Based on the electronic structures, further, the redox reactions of NCM811 can be understood. Fig. 2e–h present the PDOSs of the fully delithiated state ($Li_0Ni_{0.8}Co_{0.1}Mn_{0.1}O_2$). The charts reveal Ni^{4+}, Co^{3+}, and Mn^{4+}-like shapes, which indicate that the cationic redox reaction of Ni^{3+}-like to Ni^{4+} is a major cationic redox process. Additionally, Fig. 2d and 2h indicate a notable anionic redox reaction contribution from O ions. Therefore, the superior electrochemical performance of the Ni-rich NCM can be attributed to the combination of the anionic redox reactions[39,40] and the cationic redox reactions of the Ni ions in the stable crystal fields of the Co and Mn *d*-orbitals.

From a structural point of view, NCM811 suffers from severe structural changes with anisotropic distortions. Figure 3a shows the expansion and contraction of the *a* (blue left axis) and *c* (red right axis) lattice parameters as a function of the inverse Li content *x* in $Li_{1-x}Ni_{0.8}Co_{0.1}Mn_{0.1}O_2$. In the *a* direction, the lattice decreases gradually throughout the reaction from $x = 0$ to 1, whereas the lattice in the *c* direction shows non-monotonic behaviour, increasing from $x = 0.0$ to 0.75 and decreasing thereafter. In other words, the lattice parameters change in opposite directions from $x = 0.0$ to 0.75, but in the same direction thereafter. However, after $x = 0.75$, structural collapse is observed due to the rapid volume reduction, as shown in Fig. 3b, which is caused by the complete extraction of Li ions from between the transition metal layers. Therefore, the structural changes of NCM811 during electrochemical reactions are likely to be harmful to the cyclic performance due to the lattice distortions in opposing directions ($0.0 < x < 0.75$) and the volumetric collapse ($0.75 < x < 1.0$).

Heterogeneous Phase Transformation. To understand the thermodynamic phase transformations, the phase behaviours were investigated by calculating the DFT mixing enthalpies $H_{DFT}(x)$ with respect to normalized inverse Li content *x* using Eq. (1), as presented in Fig. 4a. Seven ground states are observed, including the initial ($x = 0$) and final ($x = 1$) states. The CP redox reaction of NCM811 consists of two one-phase reactions ($0.0 < x < 0.1667$; $0.3333 < x < 0.4167$) and three two-phase reactions ($0.1667 < x < 0.3333$; $0.4167 < x < 0.75$; $0.75 < x < 1.0$). To predict the electrochemical behaviour, Fig. 4b presents the OCVs based on the ground states

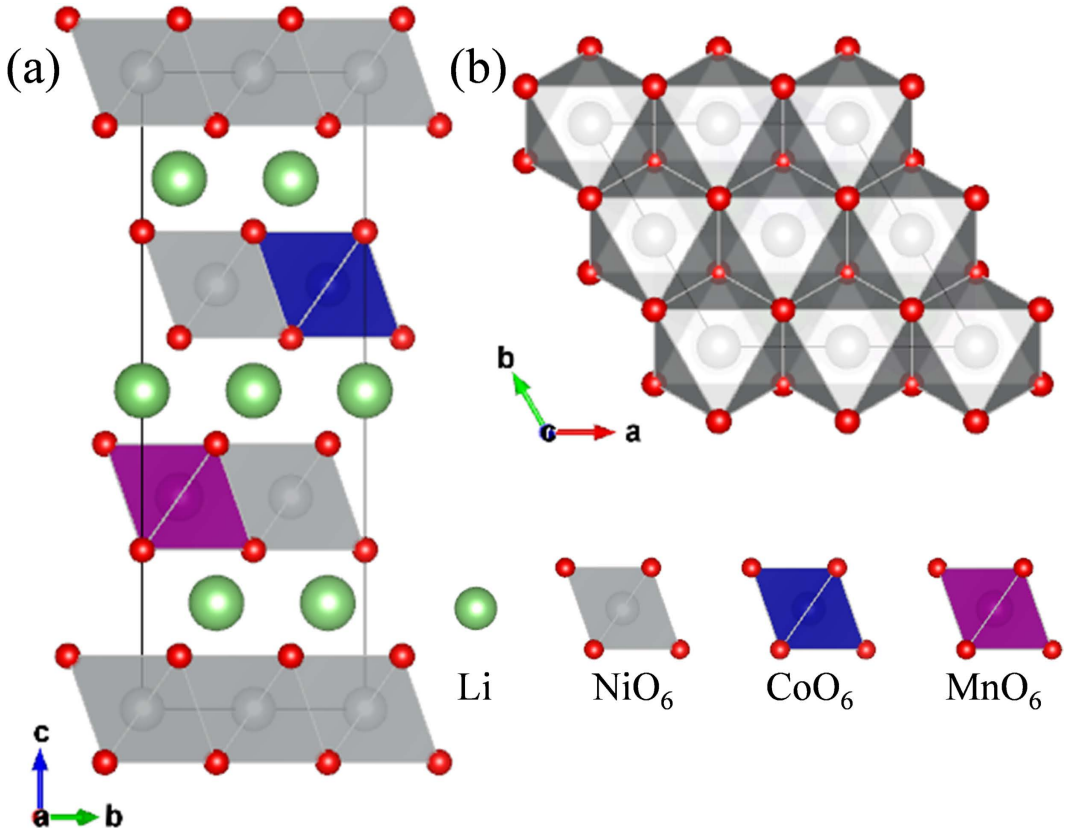

Figure 1. Atomic models of Ni-rich $LiNi_{0.8}Co_{0.1}Mn_{0.1}O_2$ (NCM811) layered oxide (*R*-3*m*) projected onto the (**a**) *bc* and (**b**) *ab* planes.

in Fig. 4a; the shape of the curve is similar to the experimental OCV values for $LiNiO_2$ estimated previously by the galvanostatic intermittent titration technique (GITT)[30].

By considering the configurational entropy at a finite temperature (300 K), more general phase behaviours can be understood using the CP free energy $f_{CP}(x)$ and the CP chemical potential μ_{CP} of Eqs (2) and (3), as shown in Fig. 5. Spinodal regions, where two-phase reactions occur, are indicated as green shaded regions in Fig. 5. Figure 5a shows that the first and second phase barriers from $x = 0.21$ to 0.30 and from $x = 0.50$ to 0.67 are low, but the third phase barrier from $x = 0.81$ to 0.93 is remarkably steep and higher than the others. This means that phase separations are likely to be impeded due to the low phase barriers and the low slopes of the chemical potentials before $x = 0.75$, such that relatively smooth reactions similar to the one-phase reaction can be generated, rather than the two-phase reaction. In contrast, after $x = 0.75$, rapid phase separation by a two-phase reaction is likely to occur as indicated by the higher phase barrier in Fig. 5a and the sharp slope of the chemical potential in Fig. 5b. More importantly, the strong phase separation after $x = 0.75$ results in a highly Li-deficient phase ($Li_0Ni_{0.8}Co_{0.1}Mn_{0.1}O_2$), leading to severe structural transformations to inactive phases such as the NiO rock salt phase previously observed by *ex situ* transmission electron microscopy in Ni-rich NCM[7].

Origins of Crack Generation. To describe the meso-scale phase transformations of $LiNi_{0.8}Co_{0.1}Mn_{0.1}O_2$ in a nanodomain with dimensions of 31.36 nm × 31.36 nm at 300 K, a phase-field model analysis was conducted by solving Eqs (9) and (10). As simulation parameters, we set D as 10^{-8} cm^2 s^{-1} based on an experimental value[41], λ as 0.49 nm from the interlayer distance of the atomic model, and the ε_i^f values as $\varepsilon_{0.1667}^{0.3333} = 128.66$ eV, $\varepsilon_{0.4167}^{0.75} = 7.85$ eV, and $\varepsilon_{0.75}^{1.0} = 169.95$ eV. The phase transformation simulations were carried out on the *ac* plane during relaxation from the solid solution at $x = 0.65$ (Fig. 6a) with a theoretical charge capacity of ~179 mAh g^{-1} and $x = 0.85$ (Fig. 6e) with a theoretical charge capacity of ~234 mAh g^{-1}. The *a*, *c*, and volumetric strains (denoted as ε_1, ε_3, and ε_V, respectively) are displayed in Fig. 6b (x = 0.65) and f (x = 0.85), 6c (x = 0.65) and 6g(x = 0.85), and 6d (x = 0.65) and 6h(x = 0.85), respectively. The strains are defined as $\varepsilon_1 = \Delta \boldsymbol{a}/\boldsymbol{a}_{x=0}$, $\varepsilon_3 = \Delta \boldsymbol{c}/\boldsymbol{c}_{x=0}$, and $\varepsilon_V = \Delta \boldsymbol{V}/\boldsymbol{V}_{x=0}$, where *a* and *c* are the lattice parameters and *V* is the volume, respectively. Finally, 2D diffusion in the *a* and *b* directions was applied, and the phase separation was triggered by random noise.

From the distribution of the inverse Li concentration, distinct phase separation is observed in Fig. 6e at $x = 0.85$, correlated with the sharp slope of the chemical potential in Fig. 5b, but only slight phase separation is observed in Fig. 6a at $x = 0.65$. For this reason, smooth electrochemical reactions may be possible until $x = 0.65$ (~179 mAh g^{-1}), but phase separation to an inactive phase ($Li_0Ni_{0.8}Co_{0.1}Mn_{0.1}O_2$) should occur at $x = 0.85$ (~234 mAh g^{-1}), meaning that the third spinodal region from $x = 0.81$ to 0.93 induces intrinsically irreversible

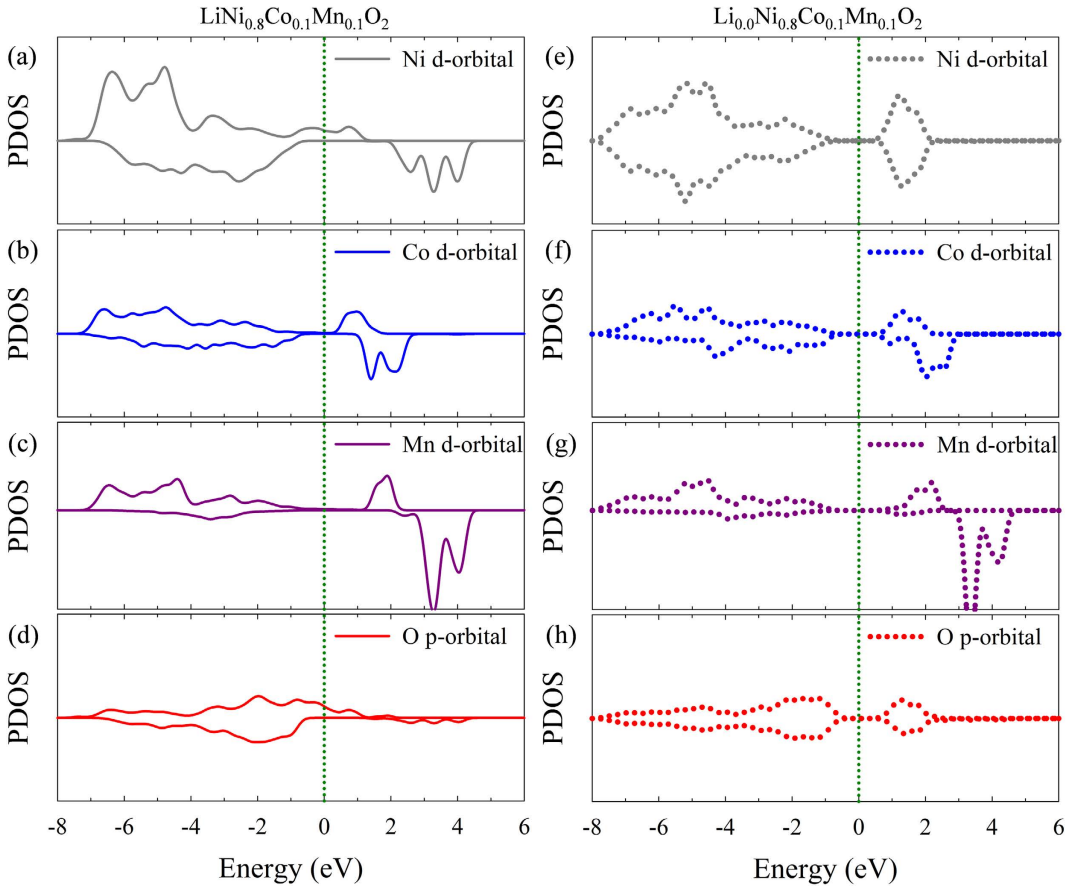

Figure 2. (**a,b,c,d**) Partial density of states (PDOSs) of (a) Ni *d*- (gray solid line), (**b**) Co *d*- (blue solid line), (**c**) Mn *d*- (purple solid line), and (**d**) O *p*- (red solid line) orbitals in $LiNi_{0.8}Co_{0.1}Mn_{0.1}O_2$. (**e,f,g,h**) PDOSs of (**e**) Ni *d*- (gray dashed line), (f) Co *d*- (blue dashed line), (**g**) Mn *d*- (purple dashed line), and (h) O *p*- (red dashed line) orbitals in $Li_{0.0}Ni_{0.8}Co_{0.1}Mn_{0.1}O_2$. The Fermi level is 0.0 eV (green dotted line).

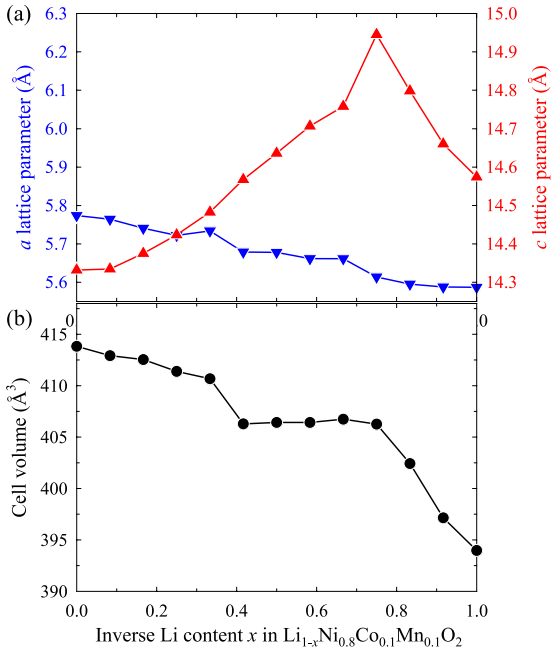

Figure 3. (**a**) Calculated *a* (blue inverse triangles and solid line, left axis) and *c* lattice parameters (red triangles and solid line, right axis), and (**b**) volume of cell (black circles and solid line) with respect to the inverse Li content *x* in $Li_{1-x}Ni_{0.8}Co_{0.1}Mn_{0.1}O_2$.

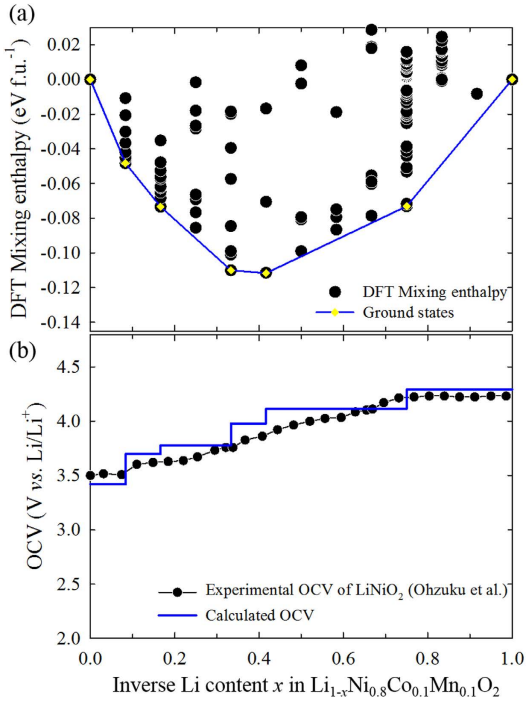

Figure 4. (**a**) Mixing enthalpies from density functional theory (DFT) calculations (black circles) with ground states (yellow diamonds and blue line). (**b**) Open-circuit voltage (OCV) calculated using first principles (blue solid line) and reproduced by experiment (black circles and line) from Ohzuku *et al*[30]. versus inverse Li content x in $Li_{1-x}Ni_{0.8}Co_{0.1}Mn_{0.1}O_2$.

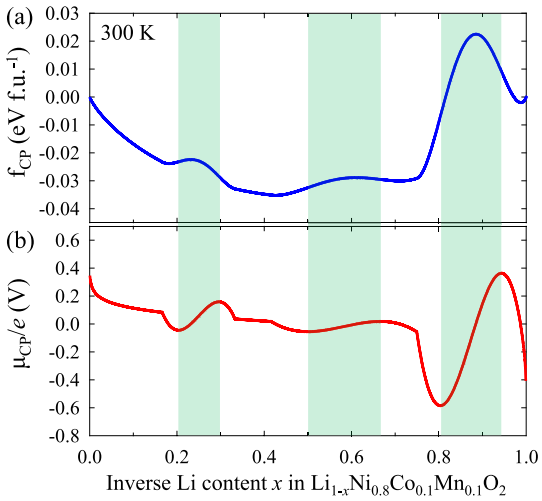

Figure 5. (**a**) Combined-phase (CP) free energy (blue solid line) and (**b**) CP chemical potential (red solid line) at room temperature (300 K) with spinodal regions (green shaded areas) with respect to inverse Li content x in $Li_{1-x}Ni_{0.8}Co_{0.1}Mn_{0.1}O_2$.

characteristics. Furthermore, from a structural perspective, at $x = 0.65$, not only are contraction strains of ε_1 and ε_3 observed, but also slight differences occur between ε_1 ($-6 \times 10^{-6} < \varepsilon_1 < -6 \times 10^{-7}$) and ε_3 ($0.027 < \varepsilon_3 < 0.028$), as shown in Fig. 6b and c. Fortunately, the extent of structural change can be considered as reasonably small; e.g., the difference in ε_V is less than 4×10^{-4}, as illustrated in Fig. 6d. Severe structural distortions occur at $x = 0.85$. All the absolute changes in the three strains at $x = 0.85$ are remarkably larger than those at $x = 0.65$: ε_1 changes relatively slightly ($-0.032 < \varepsilon_1 < -0.027$), whereas ε_3 and ε_V vary by as much as 5% ($0.018 < \varepsilon_3 < 0.043$, $-0.047 < \varepsilon_V < -0.018$) (Fig. 6f,g and h, respectively). Videos attached in the supplementary information illustrate the specific evolution of the inverse concentration of Li and the volumetric strain.

In the meso-scale phase transformation phenomena, the structural distortions are heterogeneously generated in the nanodomain due to the blocking of diffusion in the c direction and the rapid phase separation, which is

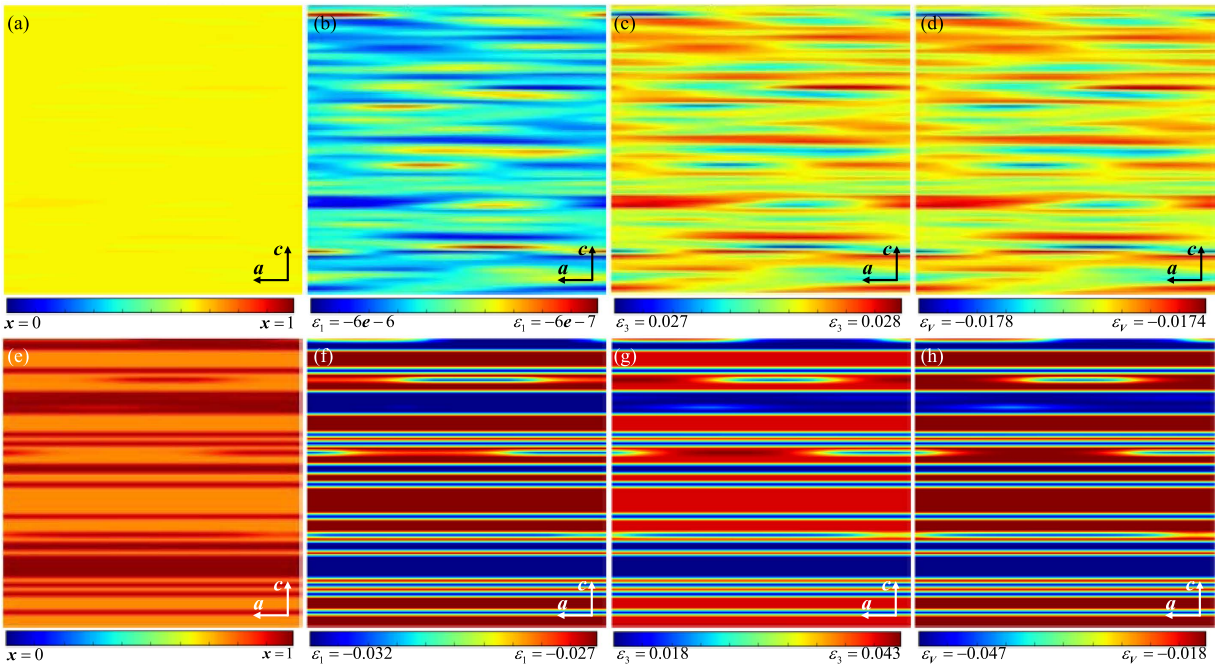

Figure 6. Meso-scale phase transformations in the nanodomain with dimensions of 31.36 × 31.36 nm in $Li_{1-x}Ni_{0.8}Co_{0.1}Mn_{0.1}O_2$ at room temperature (300 K) from a solid solution of inverse Li concentration x = 0.65 (**a,b,c,d**) and 0.85 (**e,f,g,h**) at dimensionless time $\hat{t} = 5$. (**a,e**), (**b,f**), (**c,g**), and (**d,h**) are the distributions on the *ac* plane of the inverse Li concentration *x*, strain in *a* direction ε_1, strain in *c* direction ε_3, and volumetric strain ε_V, respectively.

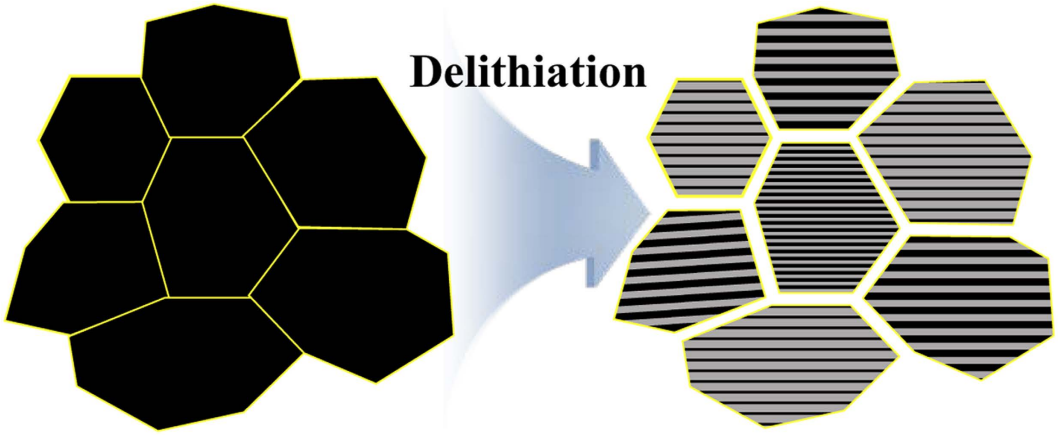

Figure 7. Schematic illustration of micro-crack generations in secondary particles on the interfaces of the contracted primary particles during delithiation.

shown in the apparent red and blue regions of Fig. 6f,g and h. Therefore, the structural changes in NCM811 occur more severely in the third spinodal region, and, combined with the abrupt phase separation, limit the intrinsic specific capacity to less than 220 mAh g^{-1} for $x = 0.81$. As shown in Fig. 7, the around 5% of anisotropic contraction and the ~3.9% of average contraction (Fig. 6h) in the nanodomain would cause the contraction of each primary particle, and then the gaps between the primary particles would result in the micro-crack generations in the secondary particles on the interfaces between the primary particles, which could be the origins and mechanism on the experimental observations of the micro-crack propagations[25–29]. Further, the heterogeneous distribution of the anisotropic strain changes causes the severe mechanical instability of the primary particles that could induce the generation of nano-cracks, which could be a crack opening of the micro-cracks.

In addition, Table 1 shows critical energy release rates of $Li_1Ni_{0.8}Co_{0.1}Mn_{0.1}O_2$ and $Li_0Ni_{0.8}Co_{0.1}Mn_{0.1}O_2$ calculated by DFT, which describe the critical energy for the crack generation and are related to the surface energy γ for brittle materials ($G_c = 2\gamma$) based on Griffith's theory. Though fully-lithiated NCM811 has low G_c (2.4308 J m^{-2}), the delithiated NCM811 has even lower G_c (−0.0064 J m^{-2}), which would result from the structural instability

	$Li_1Ni_{0.8}Co_{0.1}Mn_{0.1}O_2$	$Li_0Ni_{0.8}Co_{0.1}Mn_{0.1}O_2$
G_c	$2.4308\,J\,m^{-2}$	$-0.0064\,J\,m^{-2}$

Table 1. Critical energy release rates G_c for a crack generation of $Li_1Ni_{0.8}Co_{0.1}Mn_{0.1}O_2$ and $Li_0Ni_{0.8}Co_{0.1}Mn_{0.1}O_2$ based on Griffith's theory.

between layers at lower Li concentrations. In other words, not only NCM811 is fragile to crack generation, but also it gets weakened at delithiated states, which means the 5% of anisotropic contraction could be enough to generate crack propagations.

Recently, Meng *et al.* reported that the severe crack generation in NCM811 particles induces a significant performance degradation[29]. According to the scanning electron microscopy (SEM) observation, particle fractures and fragmentation of NCM811 particles were evident after cycles. Due to this crack generation, the discharge capacity of NCM811 was remarkably decreased with increasing overpotentials during cycles. From our fundamental understanding, we suggest that the origin of crack generation is the contraction of primary particles with a mechanical instability caused by heterogeneous phase transformation and anisotropic strain changes. In addition, the lower G_c at delithiated states contributes to a severe crack propagation. Finally, it is expected that these could be resolved by reducing the inhomogeneity and anisotropy of structural changes and increasing G_c.

Conclusion

The intrinsic limitations of a Ni-rich NCM811 cathode material were investigated in terms of its phase transformations and structural distortions using multiscale approaches combining first-principles calculations and the CP phase-field model. The major redox mechanism of NCM811 was determined as a combination of the cationic redox reactions of Ni with the anionic redox reactions of O. The atomic-scale structural analysis showed that opposite lattice changes are generated until $x = 0.75$, followed thereafter by the gradual decrease all of the lattice parameters due to the collapse of the transition metal layers. The CP behaviours represent the three two-phase reaction regions, wherein the third exhibits a higher phase barrier and a sharp rise in the chemical potential. This causes rapid phase separation, forming an inactive and highly Li-deficient phase. In the meso-scale phase transformation, heterogeneous phase separations are observed, and severe phase transformation occurs near the third spinodal region at $x = 0.85$. Further, the ~3.9% of the average contraction and lower critical energy release rates including the heterogeneous distribution of the anisotropic strain changes observed by the meso-scale strain distributions could induce not only the nano-cracks in the nanodomain of the primary particles from the severe mechanical instability, but also the micro-crack generations on the interfaces between the contracted primary particles. Thus, the combination of the abrupt transformations to inactive phases with the heterogeneous collapse of the layered structure limits the intrinsic performance of NCM811. These findings may help to predict the maximum performance of Ni-rich NCM cathodes, and the mechanistic insights on the phase transformations and structural distortions could provide clues toward improving cathode materials for battery applications.

Methodology

First-principles calculations. For the atomic-scale simulations, first-principles calculations were conducted using spin-polarized density functional theory (DFT) with the generalized gradient approximation (GGA) according to the Perdew-Wang 91 exchange-correlation functional[42]. The Vienna *Ab Initio* Simulation Package (VASP) was utilized to implement a plane-wave basis set and the projector-augmented wave (PAW) method[43,44]. To evaluate accurate electrochemical and *d*-orbital electronic properties, the Hubbard *U* parameter was used[45]. The *U* values for Ni, Co, and Mn (6.7, 4.91, and 4.64, respectively) were chosen from previous reports[37,46]. As computational parameters, a plane-wave cut-off energy of 500 eV and *k*-point meshes of $4 \times 4 \times 2$ for the Brillouin zone sampling were determined by a convergence test. The atomic model for NCM811 was developed by the 12 formula units (*f.u.*) of $LiNi_{0.8333}Co_{0.0833}Mn_{0.0833}O_2$ using high-throughput calculations[31–35]. All the calculations were based on fully relaxed structures.

Combined-phase (CP) phase transformation mechanics. For the multiscale analyses from the atomic- to meso-scale, we adopted the CP transformation model[47,48] and the Cahn-Hilliard equation[49].

First, the DFT mixing enthalpy $H_{DFT}(x)$ with respect to the normalized inverse Li content x from 0.0 to 1.0 for battery electrodes can be defined as follows:

$$H_{\mathrm{DFT}}(x) = E^{DFT}_{Li_{1-x}Ni_{0.8}Co_{0.1}Mn_{0.1}O_2} - (1-x)E^{DFT}_{Li_1Ni_{0.8}Co_{0.1}Mn_{0.1}O_2} - xE^{DFT}_{Li_0Ni_{0.8}Co_{0.1}Mn_{0.1}O_2,} \quad (1)$$

where $E^{DFT}_{Li_{1-x}Ni_{0.1}Co_{0.1}Mn_{0.1}O_2}$ represents the total energy of $Li_{1-x}Ni_{0.8}Co_{0.1}Mn_{0.1}O_2$ as calculated from DFT calculations. From the convex hull analysis of $H_{DFT}(x)$, the CP free energy $f_{CP}(x)$ and the CP chemical potential μ_{CP} at finite temperature by considering the configurational entropy[50] can be determined based on the CP mixing enthalpy $H_{CP}(x)$ as follows:

$$f_{CP}(x) = H_{CP}(x) + k_BT(x\ \ln\ x + (1-x)\ln(1-x)), \quad (2)$$

$$\mu_{CP} = -\partial f_{CP}/\partial x, \quad (3)$$

$$H_{CP}(x) = \sum \varepsilon_i^f (x - x_i)^2 (x_f - x)^2,\ x_i \le x \le x_f, \tag{4}$$

where, k_B and T represent the Boltzmann constant and absolute temperature, respectively. Furthermore, the enthalpy coefficient ε_i^f in the reaction regions from x_i to x_f is obtained by parameterization from the CP mixing enthalpy $H_{CP}^{i,f}(x)$ as follows:

$$\begin{aligned} H_{CP}^{i,f}(x) \;=\; & E^{DFT}_{Li_{1-x}Ni_{0.8}Co_{0.1}Mn_{0.1}O_2} \\ & - \frac{x - x_i}{x_f - x_i} E^{DFT}_{Li_{1-x_f}Ni_{0.8}Co_{0.1}Mn_{0.1}O_2} \\ & - \frac{x_f - x}{x_f - x_i} E^{DFT}_{Li_{1-x_i}Ni_{0.8}Co_{0.1}Mn_{0.1}O_2.} \end{aligned} \tag{5}$$

The open-circuit voltage (OCV) V_{DFT} was calculated using DFT at 0 K as follows:

$$V_{DFT}^{i,f} = \sum_{(x_i, x_f)} - \frac{\left(E^{DFT}_{Li_{1-x_f}Ni_{0.8}Co_{0.1}Mn_{0.1}O_2} - E^{DFT}_{Li_{1-x_i}Ni_{0.8}Co_{0.1}Mn_{0.1}O_2} - (x_f - x_i)\mu_{Li} \right).}{(x_f - x_i)e} \tag{6}$$

To solve the meso-scale phase transformation phenomena, the CP Cahn-Hilliard energy function G_{CP} was defined as follows:

$$G_{CP} = \int_V \rho_n \left\{ f_{CP} + \frac{\kappa_i^f}{2} |\nabla x|^2 \right\} dV, \tag{7}$$

where, ρ_n represents the number of sites per volume V and κ_i^f is the gradient energy coefficient determined by the characteristic length λ and enthalpy coefficient ε_i^f as follows:[51,52]

$$\kappa_i^f = \frac{2}{3} \lambda^2 \varepsilon_i^f. \tag{8}$$

We applied the semi-implicit Fourier-spectral method[53] with a periodic boundary condition (PBC) to compute the Cahn-Hilliard equation[49]. For non-dimensionalization, k_BT, λ, and D/λ_2 were used as the dimensionless energy, length, and time scales with the use of the diffusion coefficient D, respectively. Based on these dimensionless parameters, the Cahn-Hilliard equation can be written as follows:

$$\frac{\partial x}{\partial \hat{t}} = \hat{\nabla}^2 \left(\frac{\partial \hat{f}_{CP}(x)}{\partial x} + \hat{\kappa}_i^f \hat{\nabla}^2 x \right) = \hat{\nabla}^2 \left(h(x) + \hat{\kappa}_i^f \hat{\nabla}^2 x \right). \tag{9}$$

Then, Eq. (9) can be re-written on the Fourier space with a wave vector k as follows:

$$\frac{\partial x_k}{\partial \hat{t}} = -k^2 h_k - \hat{\kappa}_i^f k^4 x_k. \tag{10}$$

References

1. Liu, W. *et al.* Nickel-rich layered lithium transition-metal oxide for high-energy lithium-ion batteries. *Angew Chem Int Ed Engl* **54,** 4440–4457, doi: 10.1002/anie.201409262 (2015).
2. Sun, Y. K. *et al.* Nanostructured high-energy cathode materials for advanced lithium batteries. *Nat Mater* **11,** 942–947, doi: 10.1038/nmat3435 (2012).
3. Sun, Y. K. *et al.* High-energy cathode material for long-life and safe lithium batteries. *Nat Mater* **8,** 320–324, doi: 10.1038/nmat2418 (2009).
4. Armand, M. & Tarascon, J. M. Building better batteries. *Nature* **451,** 652–657, doi: 10.1038/451652a (2008).
5. Dunn, B., Kamath, H. & Tarascon, J. M. Electrical Energy Storage for the Grid: A Battery of Choices. *Science* **334,** 928–935, doi: 10.1126/science.1212741 (2011).
6. Manthiram, A., Knight, J. C., Myung, S.-T., Oh, S.-M. & Sun, Y.-K. Nickel-Rich and Lithium-Rich Layered Oxide Cathodes: Progress and Perspectives. *Advanced Energy Materials* **6,** 1501010, doi: 10.1002/aenm.201501010 (2016).
7. Jung, S.-K. *et al.* Understanding the Degradation Mechanisms of LiNi0.5Co0.2Mn0.3O2Cathode Material in Lithium Ion Batteries. *Advanced Energy Materials* **4,** 1300787, doi: 10.1002/aenm.201300787 (2014).
8. Lin, F. *et al.* Surface reconstruction and chemical evolution of stoichiometric layered cathode materials for lithium-ion batteries. *Nat Commun* **5,** 3529, doi: 10.1038/ncomms4529 (2014).
9. Kim, D. *et al.* Design of Nickel-rich Layered Oxides UsingdElectronic Donor for Redox Reactions. *Chemistry of Materials* **27,** 6450–6456, doi: 10.1021/acs.chemmater.5b02697 (2015).
10. Liang, C. *et al.* Unraveling the Origin of Instability in Ni-Rich LiNi1–2xCoxMnxO2(NCM) Cathode Materials. *The Journal of Physical Chemistry C* **120,** 6383–6393, doi: 10.1021/acs.jpcc.6b00369 (2016).
11. Chen, Z. *et al.* Hierarchical Porous LiNi1/3Co1/3Mn1/3O2 Nano-/Micro Spherical Cathode Material: Minimized Cation Mixing and Improved Li(+) Mobility for Enhanced Electrochemical Performance. *Sci Rep* **6,** 25771, doi: 10.1038/srep25771 (2016).
12. Yu, Z. *et al.* Ti-substituted Li[Li0.26Mn0.6−xTixNi0.07Co0.07]O2layered cathode material with improved structural stability and suppressed voltage fading. *J. Mater. Chem. A* **3,** 17376–17384, doi: 10.1039/c5ta03764f (2015).

13. Conry, T. E., Mehta, A., Cabana, J. & Doeff, M. M. Structural Underpinnings of the Enhanced Cycling Stability upon Al-Substitution in LiNi0.45Mn0.45Co0.1-yAlyO2 Positive Electrode Materials for Li-ion Batteries. *Chemistry of Materials* **24,** 3307–3317, doi: 10.1021/cm3011937 (2012).
14. Luo, W. B., Li, X. H. & Dahn, J. R. Synthesis, Characterization, and Thermal Stability of Li[Ni1/3Mn1/3Co1/3-z(MnMg)(z/2)]O-2. *Chemistry of Materials* **22,** 5065–5073, doi: 10.1021/cm1017163 (2010).
15. Tatsumi, K. *et al.* Local atomic and electronic structures around Mg and Al dopants in LiNiO2 electrodes studied by XANES and ELNES and first-principles calculations. *Phys Rev B* **78,** doi: ARTN 04510810.1103/PhysRevB.78.045108 (2008).
16. Cho, J., Kim, T.-J., Kim, J., Noh, M. & Park, B. Synthesis, Thermal, and Electrochemical Properties of AlPO[sub 4]-Coated LiNi[sub 0.8]Co[sub 0.1]Mn[sub 0.1]O[sub 2] Cathode Materials for a Li-Ion Cell. *Journal of The Electrochemical Society* **151,** A1899, doi: 10.1149/1.1802411 (2004).
17. Lee, Y. S., Ahn, D., Cho, Y. H., Hong, T. E. & Cho, J. Improved Rate Capability and Thermal Stability of LiNi0.5Co0.2Mn0.3O2 Cathode Materials via Nanoscale SiP2O7 Coating. *Journal of the Electrochemical Society* **158,** A1354–A1360, doi: 10.1149/2.051112jes (2011).
18. Cho, Y., Oh, P. & Cho, J. A New Type of Protective Surface Layer for High-Capacity Ni-Based Cathode Materials: Nanoscaled Surface Pillaring Layer. *Nano Lett* **13,** 1145–1152, doi: 10.1021/nl304558t (2013).
19. Jo, C. H. *et al.* An effective method to reduce residual lithium compounds on Ni-rich Li[Ni0.6Co0.2Mn0.2]O-2 active material using a phosphoric acid derived Li3PO4 nanolayer. *Nano Res* **8,** 1464–1479, doi: 10.1007/s12274-014-0631-8 (2015).
20. Mohanty, D. *et al.* Modification of Ni-Rich FCG NMC and NCA Cathodes by Atomic Layer Deposition: Preventing Surface Phase Transitions for High-Voltage Lithium-Ion Batteries. *Sci Rep* **6,** 26532, doi: 10.1038/srep26532 (2016).
21. Sun, Y. K., Myung, S. T., Kim, M. H., Prakash, J. & Amine, K. Synthesis and characterization of Li[(Ni0.8Co0.1Mn0.1)(0.8)(Ni0.5Mn0.5)(0.2)]O-2 with the microscale core-shell structure as the positive electrode material for lithium batteries. *J Am Chem Soc* **127,** 13411–13418, doi: 10.1021/ja053675g (2005).
22. Sun, Y.-K., Kim, D.-H., Jung, H.-G., Myung, S.-T. & Amine, K. High-voltage performance of concentration-gradient Li[Ni0.67Co0.15Mn0.18]O2 cathode material for lithium-ion batteries. *Electrochimica Acta* **55,** 8621–8627, doi: 10.1016/j.electacta.2010.07.074 (2010).
23. Li, Y. *et al.* Synthesis of full concentration gradient, cathode studied by high energy X-ray diffraction. *Nano Energy* **19,** 522–531, doi: 10.1016/j.nanoen.2015.07.019 (2016).
24. Park, K. J. *et al.* A high-capacity Li[Ni0.8Co0.06Mn0.14]O-2 positive electrode with a dual concentration gradient for next-generation lithium-ion batteries. *J Mater Chem A* **3,** 22183–22190, doi: 10.1039/c5ta05657h (2015).
25. Huang, R. & Ikuhara, Y. STEM characterization for lithium-ion battery cathode materials. *Current Opinion in Solid State and Materials Science* **16,** 31–38, doi: 10.1016/j.cossms.2011.08.002 (2012).
26. Miller, D. J., Proff, C., Wen, J. G., Abraham, D. P. & Bareño, J. Observation of Microstructural Evolution in Li Battery Cathode Oxide Particles by *In Situ* Electron Microscopy. *Advanced Energy Materials* **3,** 1098–1103, doi: 10.1002/aenm.201300015 (2013).
27. Zheng, S. *et al.* Microstructural Changes in LiNi0.8Co0.15Al0.05O2 Positive Electrode Material during the First Cycle. *Journal of The Electrochemical Society* **158,** A357, doi: 10.1149/1.3544843 (2011).
28. Watanabe, S., Kinoshita, M., Hosokawa, T., Morigaki, K. & Nakura, K. Capacity fade of LiAlyNi1-x-yCoxO2 cathode for lithium-ion batteries during accelerated calendar and cycle life tests (surface analysis of LiAlyNi1-x-yCoxO2 cathode after cycle tests in restricted depth of discharge ranges). *Journal of Power Sources* **258,** 210–217, doi: 10.1016/j.jpowsour.2014.02.018 (2014).
29. Meng, K., Wang, Z., Guo, H., Li, X. & Wang, D. Improving the cycling performance of LiNi0.8Co0.1Mn0.1O2 by surface coating with Li2TiO3. *Electrochimica Acta* **211,** 822–831, doi: 10.1016/j.electacta.2016.06.110 (2016).
30. Ohzuku, T., Ueda, A. & Nagayama, M. Electrochemistry and Structural Chemistry of Linio2 (R(3)over-Bar-M) for 4 Volt Secondary Lithium Cells. *Journal of the Electrochemical Society* **140,** 1862–1870, doi: 10.1149/1.2220730 (1993).
31. Hautier, G. *et al.* Novel mixed polyanions lithium-ion battery cathode materials predicted by high-throughput ab initio computations. *J Mater Chem* **21,** 17147–17153, doi: 10.1039/c1jm12216a (2011).
32. Hautier, G. *et al.* Phosphates as Lithium-Ion Battery Cathodes: An Evaluation Based on High-Throughput ab Initio Calculations. *Chemistry of Materials* **23,** 3495–3508, doi: 10.1021/cm200949v (2011).
33. Jain, A., Hautier, G., Ong, S. P., Dacek, S. & Ceder, G. Relating voltage and thermal safety in Li-ion battery cathodes: a high-throughput computational study. *Phys Chem Chem Phys* **17,** 5942–5953, doi: 10.1039/c5cp00250h (2015).
34. Morgan, D., Ceder, G. & Curtarolo, S. High-throughput and data mining with ab initio methods. *Meas Sci Technol* **16,** 296–301, doi: 10.1088/0957-0233/16/1/039 (2005).
35. Mueller, T., Hautier, G., Jain, A. & Ceder, G. Evaluation of Tavorite-Structured Cathode Materials for Lithium-Ion Batteries Using High-Throughput Computing. *Chemistry of Materials* **23,** 3854–3862, doi: 10.1021/cm200753g (2011).
36. Lim, J.-M. *et al.* The origins and mechanism of phase transformation in bulk Li2MnO3: first-principles calculations and experimental studies. *J Mater Chem A* **3,** 7066–7076, doi: 10.1039/c5ta00944h (2015).
37. Lim, J. M., Kim, D., Park, M. S., Cho, M. & Cho, K. Underlying mechanisms of the synergistic role of Li2MnO3 and LiNi1/3Co1/3Mn1/3O2 in high-Mn, Li-rich oxides. *Phys Chem Chem Phys* **18,** 11411–11421, doi: 10.1039/c6cp00088f (2016).
38. Kang, K. S., Meng, Y. S., Breger, J., Grey, C. P. & Ceder, G. Electrodes with high power and high capacity for rechargeable lithium batteries. *Science* **311,** 977–980, doi: 10.1126/science.1122152 (2006).
39. Grimaud, A., Hong, W. T., Shao-Horn, Y. & Tarascon, J. M. Anionic redox processes for electrochemical devices. *Nature Materials* **15,** 121–126, doi: 10.1038/nmat4551 (2016).
40. Sathiya, M. *et al.* Reversible anionic redox chemistry in high-capacity layered-oxide electrodes. *Nature Materials* **12,** 827–835, doi: 10.1038/Nmat3699 (2013).
41. Barker, J., Koksbang, R. & Saidi, M. Y. An electrochemical investigation into the lithium insertion properties of LixNiO2 ($0 <= x <= 1$). *Solid State Ionics* **89,** 25–35, doi: 10.1016/0167-2738(96)00262-7 (1996).
42. Perdew, J. P. *et al.* Atoms, Molecules, Solids, and Surfaces - Applications of the Generalized Gradient Approximation for Exchange and Correlation. *Phys Rev B* **46,** 6671–6687, doi: 10.1103/PhysRevB.46.6671 (1992).
43. Kresse, G. & Furthmuller, J. Efficient iterative schemes for ab initio total-energy calculations using a plane-wave basis set. *Phys Rev B* **54,** 11169–11186, doi: 10.1103/PhysRevB.54.11169 (1996).
44. Kresse, G. & Furthmuller, J. Efficiency of ab-initio total energy calculations for metals and semiconductors using a plane-wave basis set. *Comp Mater Sci* **6,** 15–50, doi: 10.1016/0927-0256(96)00008-0 (1996).
45. Hubbard, J. Electron Correlations in Narrow Energy Bands. *Proc R Soc Lon Ser-A* **276,** 238, doi: 10.1098/rspa.1963.0204 (1963).
46. Lim, J. M., Hwang, T., Park, M. S., Cho, M. Cho, K. Design of a p-type electrode for enhancing electronic conduction in high-Mn, Li-rich oxides. *Chemistry of Materials* **28,** 8201–8209 doi: 10.1021/acs.chemmater.6b03032 (2016).
47. Lim, J. M., Cho, K., Cho, M., Phase transformations with stress generations in electrochemical reactions of electrodes: Mechanics-based multiscale model for combined-phase reactions. *Extreme Mechanics Letters*, doi: 10.1016/j.eml.2016.10.008 (2016).
48. Kim, D., Lim, J. M., Park, M. S., Cho, K. & Cho, M. Phase Separation and d Electronic Orbitals on Cyclic Degradation in Li–Mn–O Compounds: First-Principles Multiscale Modeling and Experimental Observations. *ACS Applied Materials & Interfaces* doi: 10.1021/acsami.6b01595, doi: 10.1021/acsami.6b01595 (2016).
49. Cahn, J. W. & Hilliard, J. E. Free Energy of a Nonuniform System.1. Interfacial Free Energy. *J Chem Phys* **28,** 258–267, doi: Doi 10.1063/1.1744102 (1958).

50. Zhou, F., Maxisch, T. & Ceder, G. Configurational electronic entropy and the phase diagram of mixed-valence oxides: The case of LixFePO4. *Phys Rev Lett* **97,** doi: ARTN 15570410.1103/PhysRevLett.97.155704 (2006).
51. Bray, A. J. Theory of Phase-Ordering Kinetics. *Adv Phys* **43,** 357–459, doi: 10.1080/00018739400101505 (1994).
52. Han, B. C., Van der Ven, A., Morgan, D. & Ceder, G. Electrochemical modeling of intercalation processes with phase field models. *Electrochim Acta* **49,** 4691–4699, doi: 10.1016/j.electacta.2004.05.024 (2004).
53. Chen, L. Q. & Shen, J. Applications of semi-implicit Fourier-spectral method to phase field equations. *Comput Phys Commun* **108,** 147–158, doi: 10.1016/S0010-4655(97)00115-X (1998).

Acknowledgements

This study was supported by a National Research Foundation of Korea (NRF) grant funded by the Korean government (MEST) (2012R1A3A2048841), as well as by the New & Renewable Energy Core Technology Program (No. 20152020105420) funded by the Ministry of Trade, Industry & Energy (MOTIE), Republic of Korea. Computational resources for the high-throughput calculations were supported by the iBAT platform of the Industrial Strategic Technology Development Program (Grant No. 10041589) funded by MOTIE, Republic of Korea. This work was also supported by the R&D Programs of National Research Council of Science & Technology (Project No. CAP-14-2-KITECH).

Author Contributions

M.C. and J.M.L. conceived and designed this work. J.M.L., D.K. and T.H. performed the first-principles calculations. J.M.L. carried out the multiscale phase field simulations and calculated strain distributions with critical energy release rates. M.C., M.S.P., and K.C. supervised this study. M.C., K.C., M.S.P., and J.M.L. wrote the paper. All authors reviewed the manuscript.

Additional Information

Supplementary information accompanies this paper at http://www.nature.com/srep

Competing financial interests: The authors declare no competing financial interests.

How to cite this article: Lim, J.-M. *et al.* Intrinsic Origins of Crack Generation in Ni-rich $LiNi_{0.8}Co_{0.1}Mn_{0.1}O_2$ layered oxide cathode material. *Sci. Rep.* **7**, 39669; doi: 10.1038/srep39669 (2017).

Publisher's note: Springer Nature remains neutral with regard to jurisdictional claims in published maps and institutional affiliations.